

## p-type doping efficiency in CdTe: Influence of second phase formation

Jedidiah J. McCoy, Santosh K. Swain, John R. Sieber, David R. Diercks, Brian P. Gorman, and Kelvin G. Lynn

Citation: *Journal of Applied Physics* **123**, 161579 (2018);

View online: <https://doi.org/10.1063/1.5002144>

View Table of Contents: <http://aip.scitation.org/toc/jap/123/16>

Published by the [American Institute of Physics](#)

---

---

A dark blue banner with a network of glowing yellow and blue nodes and lines. The text 'Scilight' is in white and yellow. Below it, 'Sharp, quick summaries illuminating the latest physics research' is in white. A yellow button says 'Sign up for FREE!'. The AIP Publishing logo is in the bottom right.

**Scilight**

Sharp, quick summaries **illuminating**  
the latest physics research

Sign up for **FREE!**

**AIP**  
Publishing

## p-type doping efficiency in CdTe: Influence of second phase formation

Jedidiah J. McCoy,<sup>1</sup> Santosh K. Swain,<sup>1</sup> John R. Sieber,<sup>2</sup> David R. Diercks,<sup>3</sup> Brian P. Gorman,<sup>3</sup> and Kelvin G. Lynn<sup>1</sup>

<sup>1</sup>Center for Materials Research, Washington State University, Pullman, Washington 99164, USA

<sup>2</sup>National Institute of Standards and Technology, Gaithersburg, Maryland 20899, USA

<sup>3</sup>Colorado School of Mines, Golden, Colorado 80401, USA

(Received 29 August 2017; accepted 7 January 2018; published online 29 January 2018)

Cadmium telluride (CdTe) high purity, bulk, crystal ingots doped with phosphorus were grown by the vertical Bridgman melt growth technique to understand and improve dopant solubility and activation. Large net carrier densities have been reproducibly obtained from as-grown ingots, indicating successful incorporation of dopants into the lattice. However, net carrier density values are orders of magnitude lower than the solubility of P in CdTe as reported in literature,  $10^{18}/\text{cm}^3$  to  $10^{19}/\text{cm}^3$  [J. H. Greenberg, *J. Cryst. Growth* **161**, 1–11 (1996) and R. B. Hall and H. H. Woodbury, *J. Appl. Phys.* **39**(12), 5361–5365 (1968)], despite comparable starting charge dopant densities. Growth conditions, such as melt stoichiometry and post growth cooling, are shown to have significant impacts on dopant solubility. This study demonstrates that a significant portion of the dopant becomes incorporated into second phase defects as compounds of cadmium and phosphorous, such as cadmium phosphide, which inhibits dopant incorporation into the lattice and limits maximum attainable net carrier density in bulk crystals. Here, we present an extensive study on the characteristics of these second phase defects in relation to their composition and formation kinetics while providing a pathway to minimize their formation and enhance solubility. *Published by AIP Publishing.*

<https://doi.org/10.1063/1.5002144>

### INTRODUCTION

CdTe exhibits great potential for application in thin film solar cells with an optimal bandgap and a high absorption coefficient. But before this potential can be realized, the conversion efficiency must be improved as it is currently much lower than the theoretical limit, 22% as opposed to 29%.<sup>3</sup> Efforts to increase efficiency have focused on improving open circuit voltage ( $V_{oc}$ ) by addressing short minority carrier lifetime and low acceptor density in the material.<sup>4</sup> Under current circumstances, group V dopants, such as P and As, offer potential advantages because of their stability and relatively shallow acceptor behavior in CdTe.<sup>1,5</sup> In fact, recorded  $V_{oc}$  have been obtained recently in devices using P doped CdTe single crystals.<sup>4</sup> However, very limited literature exists on the study of doping efficiency of group V dopants in bulk CdTe. Hence, the mechanisms responsible for poor incorporation and subsequent activation are not well understood. Based on post growth annealing studies on P doped single crystal CdTe, defect models have been proposed where the net acceptor density has been accounted for in various Cd pressure regimes, taking into account substitutional ( $P_{Te}$ ,  $P_{Cd}$ ) defects, interstitial ( $P_i$ ) defects, and their complexes.<sup>5</sup> While the issue of dopant incorporation and activation is typically looked at from the perspective of point defects, it is equally important to study the role of second phase extended defects, especially in materials synthesized under equilibrium. Solubility studies in the past have pointed to the existence of compounds involving dopants such as  $Cd_3P_2$ ;<sup>2</sup> however, a systematic study of the genesis, distribution, and chemical composition of these secondary phases has never been performed. We conducted P doping studies on the bulk

CdTe material, which include an investigation into fundamental factors that limit dopant solubility such as secondary phases.

### EXPERIMENT

Crystals were grown in a modified vertical Bridgman furnace configuration.<sup>6</sup> The charge material consisted of 6N5 purity, solid CdTe chunks with P or  $Cd_3P_2$  powders added as dopants. When  $Cd_3P_2$  was used, solid Te shot was added to account for the excess Cd. Solid Cd or Te shot was added when excess reagents were desired. The charge material was loaded into a graphite coated, quartz ampoule or a pyrolytic boron nitride (pBN) crucible inside an uncoated quartz ampoule. To facilitate dopant incorporation into the Te sub lattice, several growths were conducted with extra Cd added to the melt. See Table I for a list of dopant concentrations and excess Cd and Te content per growth. The ampoule was evacuated down to  $\sim 10^{-5}$  Pa and simultaneously baked with infrared (IR) heaters to remove residual gases and moisture before sealing with a fitted quartz plug. After sealing, the ampoule was loaded into the vertical Bridgman furnace where growth was conducted with an imposed growth rate of 2.0 mm/h and an interface gradient of 20 °C/cm. *In situ*, post-growth cooling to room temperature was performed at rates of 7 °C/h and 25 °C/h. Growths were also quenched down to 550 °C by turning off furnace power and subsequently cooling from 550 °C to room temperature at 30 °C/h.

The grown ingot was cut into wafers and samples ( $10 \times 10 \times 2$ ) mm<sup>3</sup> for characterization. Samples for Hall effect measurements were etched for 10 min in a 2% bromine solution in methanol. Planar gold chloride or molybdenum

TABLE I. Calculated initial atomic concentrations of phosphorus and excess cadmium and tellurium per growth, alongside the measured post-growth activated densities. Activated densities taken from samples representative of the overall ingot. Uncertainty of the activated density is a combined standard uncertainty of measurement repeatability, measurements of currents and voltages, and wafer thickness.

Ingot	Doping agent	Dopant density (atoms/cm <sup>3</sup> )	Excess Cd (atoms/cm <sup>3</sup> )	Excess Te (atoms/cm <sup>3</sup> )	Activated density (holes/cm <sup>3</sup> )
A	P	$1.1 \times 10^{18}$	$6.4 \times 10^{18}$	...	$(2.24 \pm 0.04) \times 10^{15}$
B	Cd <sub>3</sub> P <sub>2</sub>	$4.5 \times 10^{18}$	$6.8 \times 10^{18}$	...	$(1.1 \pm 0.2) \times 10^{17}$
C	P	$5.6 \times 10^{17}$	$9.6 \times 10^{18}$	...	$(6.9 \pm 0.2) \times 10^{15}$
D	Cd <sub>3</sub> P <sub>2</sub>	$5.4 \times 10^{17}$	...	$1.1 \times 10^{19}$	$(6.4 \pm 0.1) \times 10^{15}$
E	Cd <sub>3</sub> P <sub>2</sub>	$3.5 \times 10^{18}$	$1.7 \times 10^{19}$	...	$(2.7 \pm 0.1) \times 10^{14}$
F	Cd <sub>3</sub> P <sub>2</sub>	$5.2 \times 10^{18}$	...	$4.0 \times 10^{18}$	$(5.7 \pm 2.2) \times 10^{16}$

dioxide contacts were evaporated on both (10 × 10) mm<sup>2</sup> surfaces per four-point probe requirements. Glow discharge mass spectrometry (GDMS) analyses were done to determine bulk ingot compositions including total phosphorus. GDMS samples (3 × 3 × 24) mm<sup>3</sup> were given a 5% bromine/methanol etch for 10 min. From each ingot, two samples were selected for GDMS at opposite ends of the ingot, the first to freeze and the last to freeze regions, or the tip and heel. Samples for depth of field infrared microscopy (IR) were prepared by polishing both (10 × 10) mm<sup>2</sup> surfaces with 1 μm de-agglomerated alumina paste on a turntable mounted polishing cloth. After characterization, the samples were annealed in Cd or Te overpressures via elemental Cd or Te pellets for up to 72 h at 600 °C to 700 °C in sealed quartz ampoules and then re-characterized. In addition, several samples were selected for energy dispersive X-ray fluorescence spectrometry (EDXRF) and energy dispersive X-ray spectroscopy in a scanning electron microscope (SEM-EDS). EDXRF spectra were collected using an Ametek EDAX Eagle 3 spectrometer and net count rates were extracted for P K-L<sub>2,3</sub>, Cd L-series, Te L-series, and scattered Rh L-series X-rays from the tube. The measurement conditions were 25 kV, 1000 μA, 15 s live time per location, and a vacuum environment. SEM-EDS data were collected using a FEI Helios 600i instrument equipped with an EDAX 60 mm<sup>2</sup> Octane Super Detector and an ion milling beam.

In summary, Hall effect measurements yielded charge carrier type and density. GDMS provided bulk compositional analysis. IR measurements were made to assess second phase content within the material. Annealing experiments revealed the effects and influence of non-stoichiometry. EDXRF and SEM-EDS generated information about the compositions of second phase defects.

## RESULTS AND ANALYSIS

Investigation of the theory that the dopant becomes incorporated into second phase defects as compounds of

cadmium and phosphorous, thereby limiting maximum attainable net carrier densities, was initiated by characterizing the net carrier densities in as-grown crystals. Hall effect measurements confirmed the p-type material and yielded net carrier density values in the 10<sup>15</sup>/cm<sup>3</sup> to low 10<sup>17</sup>/cm<sup>3</sup> range. These values represent a substantial improvement in p-type charge carrier density. However, they are still an order of magnitude lower than theoretical solubility.<sup>7</sup> In addition, these charge carrier values, inferring single acceptor dopant behavior, represent at most 2.4% of the initial dopant concentration. That small fraction suggests a substantial amount of dopant remains unaccounted for. This apparent loss of dopant could be attributed to a cancellation of p-type carriers due to a fraction of dopant acting as donors or to a physical loss of the dopant material from the primary phase.

Several interesting physical observations were made. Upon post growth opening of the sealed quartz ampoule of each P doped ingot, a white vapor was released from the crucible. This vapor was most intense directly after removal of the crucible lid and subsided within one minute. This observation coincides with the description of several P oxides and could represent a substantial loss of dopant material during the growth process. Other compounds may also fit this description, but this observation is yet to be observed in undoped CdTe grown under identical conditions. GDMS measurements revealed that up to 50% of the initial P dopant material is lost in the growth process which is a strong indication that the white vapor is a P compound, see Table II. However, GDMS measurements also indicated that P concentrations in the ingots, while significantly lower than the added concentrations, were consistently much higher than the measured net carrier density values, see Table II. In fact, activated dopant values from Hall Effect measurements accounted for at most ~5.5% of the measured GDMS concentration. Thus, physical loss of dopant during growth cannot fully account for the discrepancy.

The alternative explanation of the dopant becoming incorporated as a second phase in the ingots is consistent

TABLE II. Phosphorus atomic concentrations from GDMS compared to the initial & net carrier concentrations. Uncertainties estimated for GDMS results are 0.5 times the result to 2 times the result.

Locations:	Ingot A tip	Ingot A heel	Ingot B tip	Ingot B heel	Ingot D tip	Ingot D heel
GDMS density (atoms/cm <sup>3</sup> )	$6.5 \times 10^{17}$	$6.8 \times 10^{17}$	$2.0 \times 10^{18}$	$2.9 \times 10^{18}$	$1.5 \times 10^{17}$	$3.1 \times 10^{17}$
GDMS density/dopant density (%)	59	62	44	64	28	57
Activated density/dopant density (%)		0.2		2.4		1.2

with the high dopant results from GDMS, because GDMS analysis includes any secondary phases present in the bulk ingot. IR measurements yielded second phase inclusion density, mean diameter, and volume fraction as well as cross sectional inclusion geometries. The volume fraction of the second phase material was calculated using the mean inclusion diameter, where the 3-Dimensional inclusion shape was assumed to be spherical. Although the occurrence of second phase extended defects, or inclusions, of Cd and/or Te composition is common in CdTe, the volume fraction of the second phase content within these ingots was consistently much greater than expected. It should be noted that undoped crystal growths performed in the author's laboratory, under identical conditions of growth, stoichiometry, and cooling have resulted in inclusion free ingots as revealed by IR.<sup>8</sup> The CdTe phase diagram indicates that there exists a maximum solubility of  $\sim 5.1 \times 10^{18}$  atoms/cm<sup>3</sup> for Cd and  $\sim 1.6 \times 10^{19}$  atoms/cm<sup>3</sup> for Te in the CdTe lattice.<sup>9</sup> Any initial excess Cd or Te greater than these concentrations is expected to contribute to second phase volume. If the density of pure Cd is taken to be  $\sim 8.65$  g/cm<sup>3</sup> and pure Te to be  $\sim 6.2$  g/cm<sup>3</sup>,<sup>10</sup> then the added excess Cd and Te amounts were not sufficient to account for the observed second phase volume. This suggests not all second phase inclusions are pure Cd or Te. But it should be noted that with a Cd<sub>3</sub>P<sub>2</sub> density of 5.96 g/cm<sup>3</sup> (Ref. 10) and an initial P dopant concentration of  $4.4 \times 10^{18}$  atoms/cm<sup>3</sup>, there is not enough P dopant present to account for the total second phase volume measured per ingot if Cd<sub>3</sub>P<sub>2</sub> is assumed. At least a portion of the second phase defect volume must come from Cd, Te, polycrystalline CdTe, or voids, but likely some of each.

The second phase cross sectional geometry further supports an inclusion composition which contains the P dopant, Fig. 1. The observed two-dimensional inclusion shapes included circular, triangular, and hexagonal, but the great majority of inclusions appeared as parallelograms in the form of squares, rhomboids, and large, elongated rectangles.

This high number of parallelogram shaped inclusions was of particular interest, because it is difficult to explain in terms of traditional, native inclusion behavior.<sup>11,12</sup> As previously mentioned, CdTe often exhibits a high concentration of Cd and/or Te extended second phase defects, which have been well documented in previous research. Extended Cd defects tend to form as needle-like inclusions up to 150  $\mu\text{m}$  in length or star-like inclusions up to 100  $\mu\text{m}$  wide.<sup>9,10</sup> These large inclusions were found to be composed of clusters of smaller Cd inclusions. Both formations are dissimilar to the observed parallelogram inclusion formations here. On the other hand, extended Te defects tend to form inclusions as uniform tetrahedral structures along  $\langle 111 \rangle$  directions in the CdTe lattice.<sup>13</sup> The two-dimensional appearance is thus influenced by the angle from which it is viewed and can appear as square or rhomboidal, depending on the crystal orientation. These inclusions have been consistently found in the same grain with triangular inclusions. While Te inclusions offer a possible explanation for the observed square and rhomboidal inclusions, the observed large, elongated rectangular inclusions do not at all coincide with typical tetrahedral Te inclusion behavior even at increased dimensions. As the Te inclusion becomes larger, the corners of the tetrahedron are terminated by subsequent (111) planes, resulting in a hexagonal appearance.<sup>13</sup> Eventually, with increasing size, the inclusion will appear circular.<sup>13</sup>

Te inclusions can also form long bubble chamber threads or pearl string morphologies, as Henager<sup>13</sup> called them, through constitutional super-cooling at the solid-liquid interface. Normally, these threads appear as perforated lines with inclusions spaced evenly apart, but if particle spacing is small enough, the string will appear as a long thread. This is the most geometrically plausible explanation for the elongated rectangular inclusions. In fact, several of these large, elongated rectangular inclusions were observed in the samples of this work, where the sample surface cuts at an angle through the original inclusion [see Fig. 2]. In these cases, the

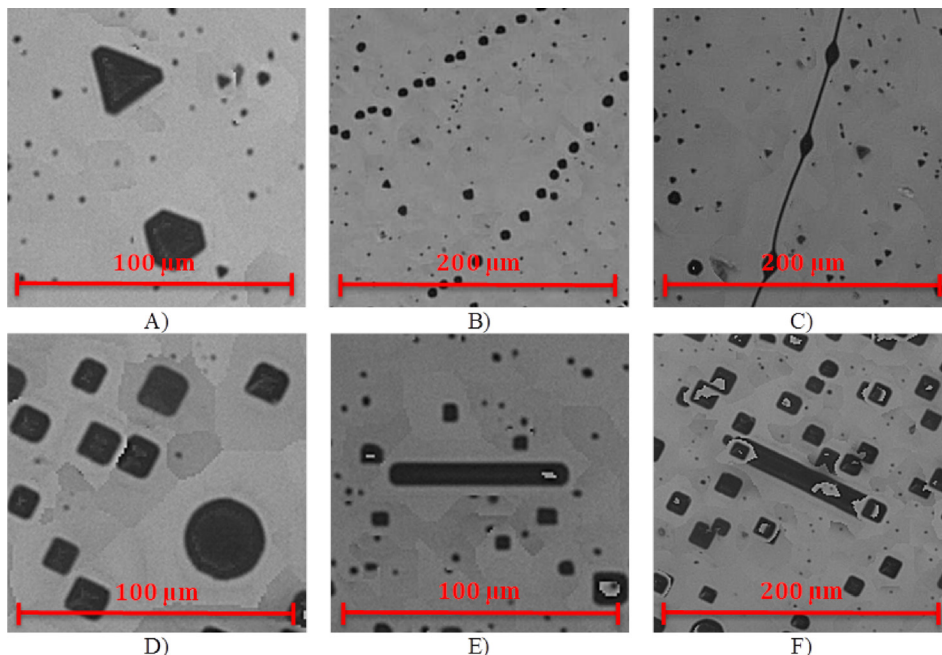


FIG. 1. IR images of (a) triangular Te inclusions, (b) separated pearl string inclusions, (c) connected pearl string inclusions, (d) square inclusions of interest, (e) elongated rectangular inclusion of interest, and (f) elongated rectangular inclusions surrounded by square inclusions.

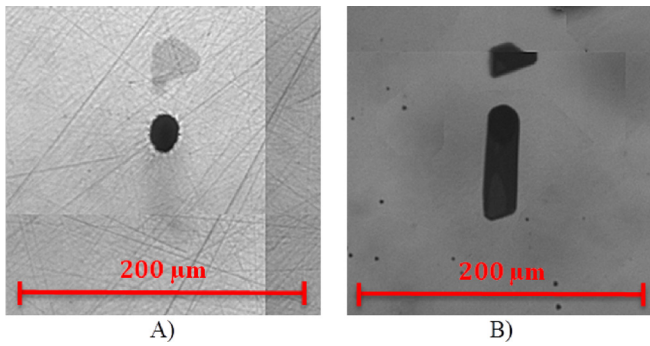


FIG. 2. (a) Cross section of elongated rectangular inclusion intersected by the sample surface and (b) IR image of same inclusion viewed at and under the surface.

inclusion cross section appears circular, indicating the three-dimensional inclusion shapes are cylindrical as would be expected in a Te thread. However, the dimensions and distributions of these elongated rectangles are unprecedented in comparison with previous CdTe growths.<sup>14</sup> Pearl string morphologies are most common and pronounced in Te rich growths, but these large, elongated rectangles were observed in Cd rich or stoichiometric growths. In contrast, Ingot D and Ingot F (Table I) were grown under excess Te conditions and resulted in much lower second phase distributions devoid of elongated rectangular inclusions.

Annealing experiments provided additional evidence that a significant portion of these rectangular inclusions are not Te-based compounds. Samples were annealed in Cd, Te, and Cd/Te environments. Figure 3 shows the inclusion volume fraction and density distributions for these experiments. Annealing in a Te rich environment decreased the second phase number and volume substantially, Fig. 3(a). One such sample exhibited a tenfold decrease in inclusion density and

nearly twentyfold decrease in inclusion volume. There is a substantial volume peak at  $12.5 \mu\text{m}$  in the as-grown sample, which is clearly visible in the logarithmic density plot. Te annealing completely removes this peak. In contrast, annealing in a Cd rich environment was shown to increase both the second phase number and volume, Fig. 3(b). One such sample exhibited an almost twofold increase in inclusion density and more than threefold increase in inclusion volume, after annealing in Cd. This is a strong indication that these inclusions are of Cd composition.

High inclusion density samples with a number of interesting inclusions and twinning planes were selected for EDXRF analyses. The twinning planes were advantageous because they increased the probability of finding inclusions at or near the location where the twinning plane intersects the sample surface. The planes can be seen in Fig. 4(a) as diagonal bands of inclusions visible to the naked eye. Figure 4(b) is a point map of the P K-L<sub>2,3</sub> peak net count rate after removal of the Te escape peak and subtraction of the background. The P K-L<sub>2,3</sub> map shows nearly 20 P-rich regions, which correspond to the pattern of twinning planes. This distribution of the P K-L<sub>2,3</sub> count rates is a strong indication of isolated P rich inclusions within a material.<sup>15</sup> The apparent dimensions of the inclusions are broadened by the relatively large diameter X-ray beam and macroscopic collimation on the detector. The more intense inclusions are larger and/or nearer the surface of the CdTe sample. Both Cd and Te L series net count rates were observed to decrease at inclusions by  $\sim 5\%$  relative to the bulk. This result was unexpected, because the inclusions are thought to be depleted in Te relative to the bulk CdTe matrix and given strong evidence of Cd based inclusion compounds. Because the microXRF measured locations are larger in volume than inclusions, some matrix CdTe was also measured. Therefore, the contrast

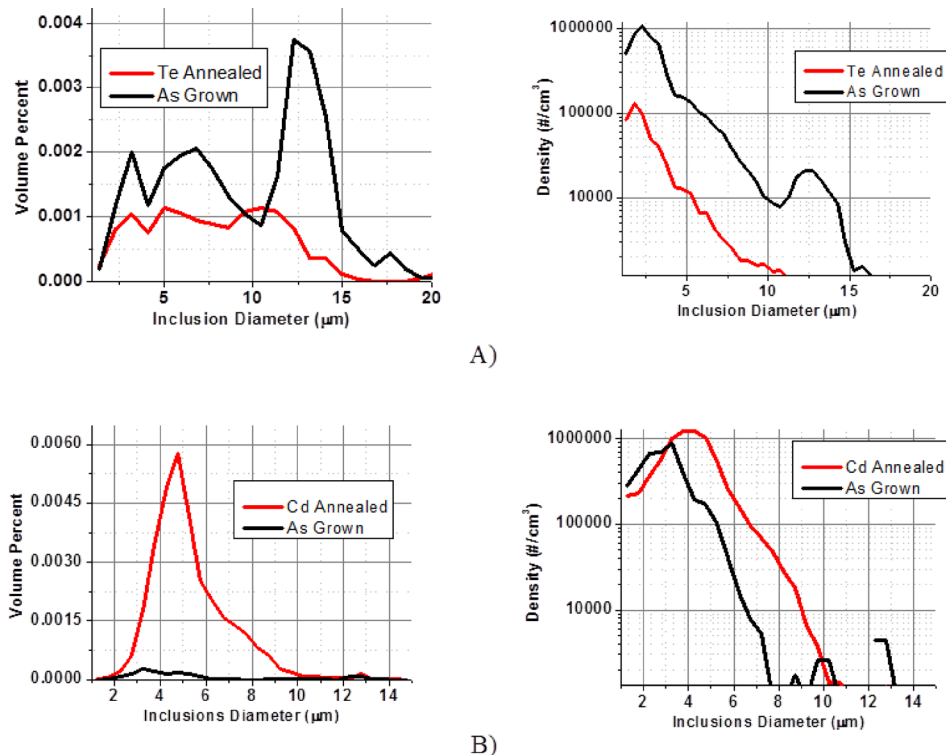


FIG. 3. Inclusion volumes and density distributions as functions of inclusion diameter for (a) Ingot A sample annealed in Te and (b) Ingot B sample annealed in Cd.

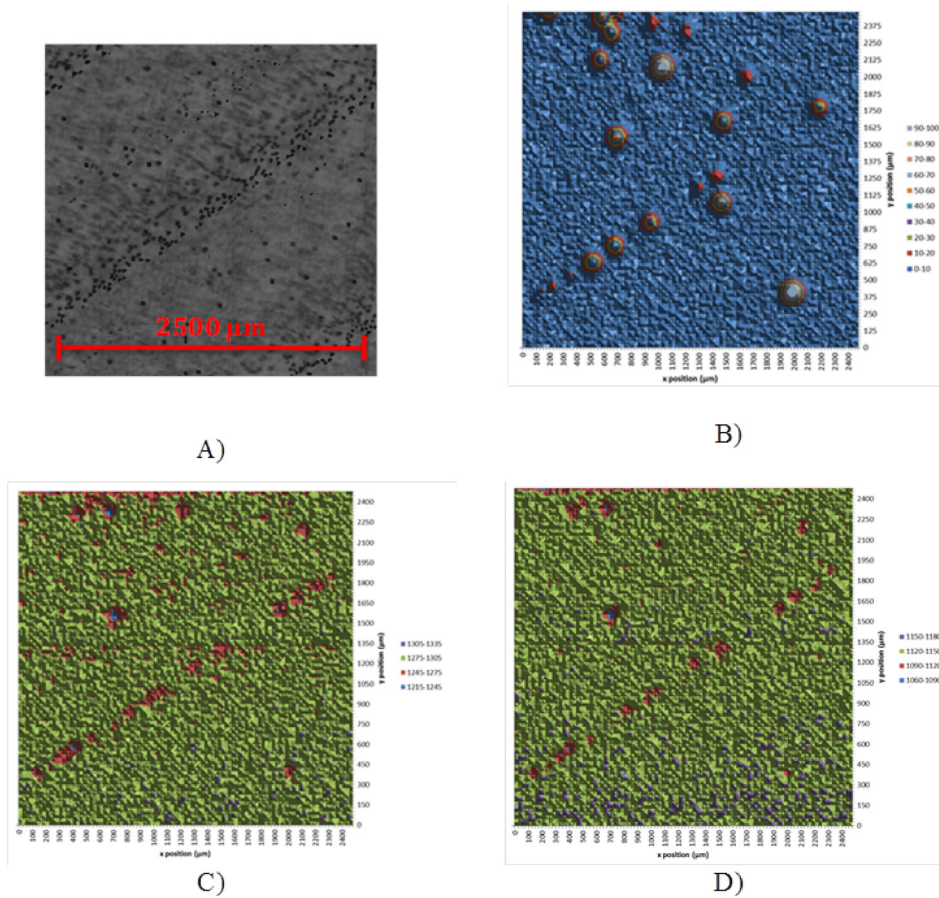


FIG. 4. (a) IR image of the sample surface & twinning planes with high inclusion density. Count rate intensity maps created from a  $100 \times 100$  points array with a nominal  $50 \mu\text{m}$  X-ray beam,  $25 \mu\text{m}$  step size, and 15 s dwell time per location for (b) P K-L<sub>2,3</sub>, (c) Cd L-series, and (d) Te L-series lines.

between the CdTe matrix and inclusions is reduced. The rhodium scatter count rate data (not shown) is sensitive to the density and average atomic number of a measured location. These data indicate small differences between inclusions and the CdTe bulk, which is consistent with low contrasts of both density and average atomic number in the measured volume for each location. The data are consistent with the presence of inclusions of  $\text{Cd}_3\text{P}_2$  ( $5.96 \text{ g/cm}^3$  vs.  $6.20 \text{ g/cm}^3$  for CdTe<sup>8</sup>).

The high absorption coefficient of CdTe for P X-rays made the information depth very shallow with an estimated total attenuation length  $< 5 \mu\text{m}$ . Estimates of attenuation lengths are given in Table III, based on calculations using an online tool.<sup>16</sup> The information depths for Cd and Te are much greater than P which may explain why the Te signal did not go to zero at the inclusion centers. Also, Te has an escape peak that falls directly on the P K-L<sub>2,3</sub> peak making detection of low P concentrations in the bulk ingot ( $4.4 \times 10^{18}$  atoms/ $\text{cm}^3$  for Ingot B) difficult, if not impossible with a Si(Li)

detector, as used here. Detection of P would only be expected for localized regions enriched in P concentration relative to the bulk.

SEM-EDS measurements were taken on specific inclusions in a sample from Ingot B to overcome the resolution and depth limitations encountered in XRF measurements. The focused ion beam was used to mill down to subsurface inclusions, effectively eliminating the possibility of contaminants or loss of inclusion material during sample processing. The results confirm the presence of increased P concentrations at the inclusions. Figure 5 shows point maps for P, Cd, and Te from a specific inclusion. The trench walls prevented a portion of X-rays from reaching the detector. This resulted in a shadowing effect on the lower right-hand side in all three point maps that is most apparent in the P point map likely due to the relatively low energy of the P X-rays. Both Cd and Te signals appear to diminish equally and substantially at the inclusion region relative to the CdTe bulk region.

Finally, *in situ*, post-growth cooling demonstrated a strong influence on the formation of second phase inclusions. Fast cooled growths,  $\geq 25 \text{ }^\circ\text{C/h}$ , yielded a substantial decrease in the mean inclusion diameter and overall second phase volume indicating that slow cooling promoted secondary phase growth. All quenched growths were free of elongated rectangular inclusions. Inclusion free crystals were achieved in Ingot E, a growth performed under high excess Cd and fast cooling conditions, Fig. 6. Ingot E exhibited relatively low dopant activation. The highest carrier density was achieved in Ingot F, a quenched growth grown in excess Te. The carrier

TABLE III. K-L<sub>2,3</sub> and L-series lines for P, Cd, & Te and approximate attenuation lengths in CdTe.

Element	Line	Line energy (eV)	Attenuation length ( $\mu\text{m}$ )	100% attenuation ( $\mu\text{m}$ )
P	K-L <sub>2,3</sub>	2015	0.99	4.6
Cd	L	3133	3.1	14
Te	L	3769	1.9	8.7
Cd	K-L <sub>2,3</sub>	23 109	120	540
Te	K-L <sub>2,3</sub>	27 380	58	270

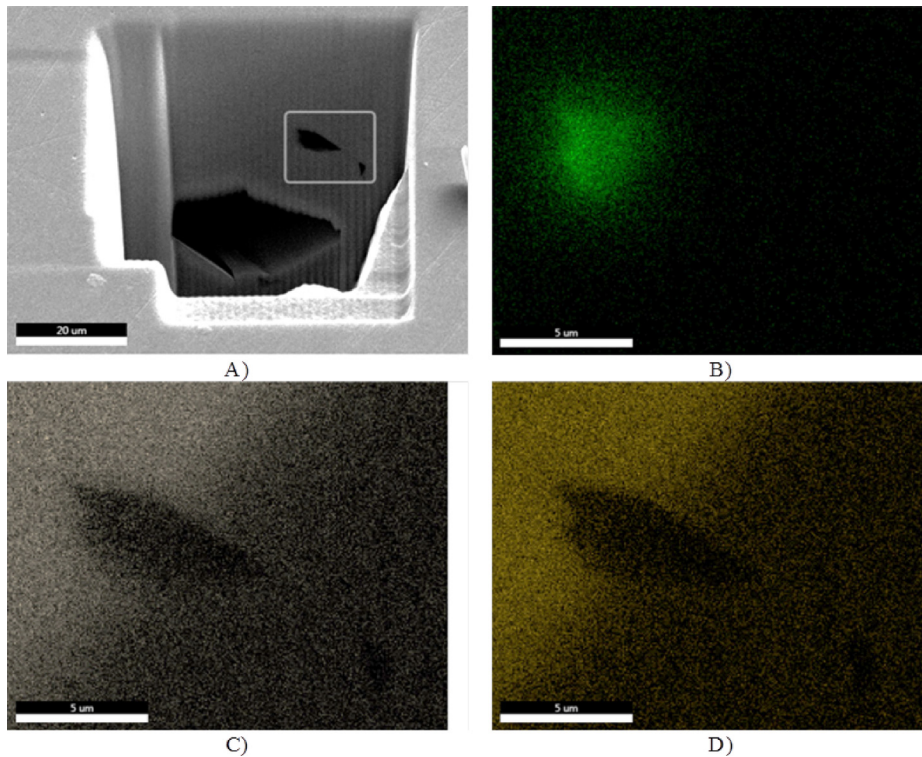


FIG. 5. (a) SEM image of the ion-milled sample region and measured inclusion, (b) P intensity point map, (c) Cd intensity point map, and (d) Te intensity point map.

density results between Ingot E and Ingot F are counterintuitive as growth in excess Cd is expected to result in more Te vacancies and thus more activated P atoms. This result is perhaps indicative of compensation by native defects such as Cd interstitials and Te vacancies beyond certain Cd pressures. The compensation by Cd interstitials was discussed in the defect model developed by Selim and Kröger,<sup>5</sup> whereas recently, the shallow donor behavior of Tellurium vacancies has been reported.<sup>17,18</sup> Also note that annealing in Te revealed a substantial decrease in second phase defects shown to contain the P dopant. It is then recommended that growth in slightly excess Te is necessary to inhibit dopant loss to second phase defects.

## CONCLUSIONS

This study provides one explanation for the difficulty in attaining theoretical p-type net carrier density values in CdTe crystals grown in equilibrium conditions. While as much as 50% of the dopant material was initially lost to the atmosphere, GDMS data in comparison to the Hall effect data indicated that a large fraction of the dopant remained

within the ingot, either electrically inactive or neutralized. IR data revealed a plethora of geometrically abnormal inclusions, difficult to explain in terms of intrinsic inclusion behavior. These inclusions were later revealed by annealing experiments to likely be of Cd composition. XRF was implemented to observe the relative count rates in the vicinities of high interest inclusions and provided evidence of a Cd containing the P phase in the inclusions. SEM-EDS confirmed the presence of P within these inclusions, but could not provide conclusive evidence of Cd within the inclusions.

In conclusion, the P dopant can become incorporated into second phase defects, most likely as  $\text{Cd}_3\text{P}_2$ , limiting the electrical effectiveness of the dopant. With this information, growth optimization can focus on inhibiting the formation of these defects to ensure better dopant incorporation and activation. In addition, it was shown that proper post-processing, annealing regimes, as well as growth parameter manipulation in terms of stoichiometry, cooling rate, etc., can be developed for maximizing solubility.

## ACKNOWLEDGMENTS

This work was supported by the U.S. Department of Energy under Contract No. DE-AC36-08-GO28 with the National Renewable Energy Laboratory. This material is based upon work supported by the U.S. Department of Energy, Office of Energy Efficiency and Renewable Energy (EERE), under Award No. DE-EE0007537.

Certain commercial items are identified in this document to adequately specify the experimental procedures. Such identification does not imply recommendation or endorsement by the National Institute of Standards and Technology, nor does it imply that the materials or equipment identified are necessarily the best available for the purpose.

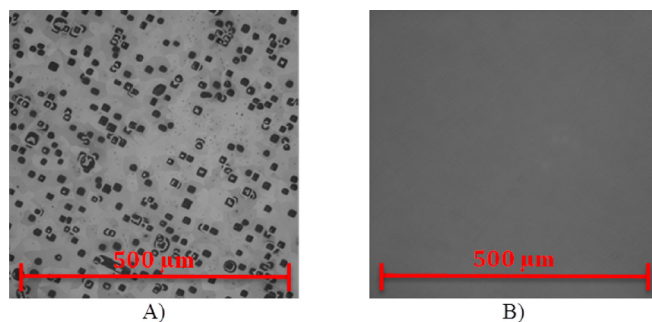


FIG. 6. IR images of (a) Ingot B with a high inclusion content and (b) Ingot E free of inclusions.

- <sup>1</sup>J. H. Greenberg, “P-T-X phase equilibrium and vapor pressure scanning of non-stoichiometry in CdTe,” *J. Cryst. Growth* **161**, 1 (1996).
- <sup>2</sup>R. B. Hall and H. H. Woodbury, “The diffusion and solubility of phosphorus in CdTe and CdSe,” *J. Appl. Phys.* **39**(12), 5361–5365 (1968).
- <sup>3</sup>A. Kanevce and T. A. Gessert, “Optimizing CdTe solar cell performance: Impact of variations in minority-carrier lifetime and carrier density profile,” *J. Photovoltaics* **1**(1), 99–103 (2011).
- <sup>4</sup>J. M. Burst *et al.*, “Interface characterization of single-crystal CdTe solar cells with  $V > 950$  mV,” *IEEE J. Photovoltaics* **6**(6), 1650–1653 (2016).
- <sup>5</sup>F. A. Selim and F. A. Kröger, “The defect structure of CdTe,” *J. Electrochem. Soc.* **124**(3), 401–408 (1977).
- <sup>6</sup>S. Sen, W. H. Konkel, S. J. Tighe, L. G. Bland, S. R. Sharma, and R. E. Taylor, “Crystal growth of large-area single-crystal CdTe and CdZnTe by the computer-controlled vertical modified-Bridgman process,” *J. Cryst. Growth* **86**(1–4), 111–117 (1988).
- <sup>7</sup>U. V. Desnica, “Doping limits in II–VI compounds—Challenges, problems and solutions,” *Prog. Cryst. Growth Charact. Mater.* **36**(4), 291–357 (1998).
- <sup>8</sup>S. K. Swain *et al.*, “Bulk growth of uniform and near stoichiometric cadmium telluride,” *J. Cryst. Growth* **389**, 134–138 (2014).
- <sup>9</sup>V. N. Guskov, J. H. Greenberg, M. Fiederle, and K. W. Benz, “Vapour pressure investigation of CdZnTe,” *J. Alloys Compd.* **371**(1–2), 118–121 (2004).
- <sup>10</sup>W. M. Haynes, *CRC Handbook of Chemistry and Physics*, 93rd ed., revise ed. (CRC Press, Boca Raton, Florida, 2016).
- <sup>11</sup>P. Rudolph, A. Engel, I. Schentke, and A. Grochocki, “Distribution and genesis of inclusions in CdTe and (Cd,Zn)Te single crystals grown by the Bridgman method and by the travelling heater method,” *J. Cryst. Growth* **147**(3–4), 297–304 (1995).
- <sup>12</sup>P. Yu and W. Jie, “Observation, morphology evolution and elimination of Te inclusions in CdZnTe: In single crystals,” *J. Cryst. Growth* **381**, 57–60 (2013).
- <sup>13</sup>C. Henager, K. J. Alvine, M. Bliss, B. J. Riley, and J. A. Stave, “The influence of constitutional supercooling on the distribution of Te-particles in melt-grown CZT,” *J. Electron. Mater.* **44**(11), 4604–4621 (2015).
- <sup>14</sup>S. Bhaladhare *et al.*, “Correlations of secondary phases (SPs) with mobility lifetime ( $\mu\tau$ ) of the electrons in CZT crystals using IR microscopy,” *Proc. SPIE* **8142**, 81421O (2011).
- <sup>15</sup>J. Molloy and J. Sieber, “Assessing microscale heterogeneity in batches of reference materials using microbeam XRF,” *X-Ray Spectrom.* **40**(4), 306–314 (2011).
- <sup>16</sup>B. L. Henke, E. M. Gullikson, and J. C. Davis, “X-ray interactions with matter, scattering, transmission, and reflection at  $E=50$ –30000 eV,  $Z=1$ –92,” see [http://henke.lbl.gov/optical\\_constants/atten2.html](http://henke.lbl.gov/optical_constants/atten2.html) for Atomic Data and Nuclear Data Tables (last accessed July 20, 2004).
- <sup>17</sup>J. Ma *et al.*, “Dependence of the minority-carrier lifetime on the stoichiometry of CdTe using time-resolved photoluminescence and first-principles calculations,” *Phys. Rev. Lett.* **111**(6), 67402 (2013).
- <sup>18</sup>D. S. Albin *et al.*, “Cd-rich and Te-rich low-temperature photoluminescence in cadmium telluride,” *Appl. Phys. Lett.* **104**(9), 92109 (2014).